

Article

Changes in Snow Surface Albedo and Radiative Forcing in the Chilean Central Andes Measured by In Situ and Remote Sensing Data

Luis Figueroa-Villanueva ^{1,*}, Lina Castro ^{1,*}, Tomás R. Bolaño-Ortiz ², Raúl P. Flores ¹,
Diego Pacheco-Ferrada ¹ and Francisco Cereceda-Balic ^{3,4}

¹ Departamento de Obras Civiles, Universidad Técnica Federico Santa María, Valparaíso 2340000, Chile

² School of Natural Resources Engineering, Department of Agricultural Science, Universidad Católica del Maule, Curicó 3466706, Chile

³ Centre for Environmental Technologies (CETAM), Universidad Técnica Federico Santa María, Valparaíso 2340000, Chile; francisco.cereceda@usm.cl

⁴ Departamento de Química, Universidad Técnica Federico Santa María, Valparaíso 2340000, Chile

* Correspondence: luis.figueroav@alumnos.usm.cl (L.F.-V.); lina.castro@usm.cl (L.C.)

Abstract: Snow-covered regions are the main source of reflection of incident shortwave radiation on the Earth's surface. The deposition of light-absorbing particles on these regions increases the capacity of snow to absorb radiation and decreases surface snow albedo, which intensifies the radiative forcing, leading to accelerated snowmelt and modifications of the hydrologic cycle. In this work, the changes in surface snow albedo and radiative forcing were investigated, induced by light-absorbing particles in the Upper Aconcagua River Basin (Chilean Central Andes) using remote sensing satellite data (MODIS), in situ spectral snow albedo measurements, and the incident shortwave radiation during the austral winter months (May to August) for the 2004–2016 period. To estimate the changes in snow albedo and radiative forcing, two spectral ranges were defined: (i) an enclosed range between 841 and 876 nm, which isolates the effects of black carbon, an important light-absorbing particle derived from anthropogenic activities, and (ii) a broadband range between 300 and 2500 nm. The results indicate that percent variations in snow albedo in the enclosed range are higher than in the broadband range, regardless of the total amount of radiation received, which may be attributed to the presence of light-absorbing particles, as these particles have a greater impact on surface snow albedo at wavelengths in the enclosed band than in the broadband band.

Keywords: snow surface albedo; radiative forcing; light-absorbing particles in snow; remote sensing; black carbon; Chilean Central Andes Mountains



Citation: Figueroa-Villanueva, L.; Castro, L.; Bolaño-Ortiz, T.R.; Flores, R.P.; Pacheco-Ferrada, D.; Cereceda-Balic, F. Changes in Snow Surface Albedo and Radiative Forcing in the Chilean Central Andes Measured by In Situ and Remote Sensing Data. *Water* **2023**, *15*, 3198. <https://doi.org/10.3390/w15183198>

Academic Editor: Hongyi Li

Received: 30 June 2023

Revised: 9 August 2023

Accepted: 17 August 2023

Published: 8 September 2023



Copyright: © 2023 by the authors. Licensee MDPI, Basel, Switzerland. This article is an open access article distributed under the terms and conditions of the Creative Commons Attribution (CC BY) license (<https://creativecommons.org/licenses/by/4.0/>).

1. Introduction

Uncontaminated snow surfaces are among the whitest surfaces on Earth and have one of the highest broadband albedos in the solar spectrum range [1]. Surface snow albedo (SSA) is a fundamental factor for the reflection of incident shortwave radiation (ISR) in the global snow–atmosphere budget system [2–5]. In the visible (VIS) and near-infrared (NIR) spectral ranges (<1 μm), SSA is strongly influenced by the presence of light-absorbing particles (LAPs), whereas for wavelengths above 1 μm, the variability of SSA is mainly controlled by the grain size of snow crystals [6,7]. The deposition of LAPs in snow darkens the surface of the snowpack, decreasing the reflection of ISR and the albedo [8–10]. Moreover, grain metamorphism is accelerated in the presence of LAPs, through a process that is typically referred to as the snow grain size feedback [11,12], which results in a higher ISR-absorbing capacity [13,14]. The deposition of LAPs increases radiative forcing (RF) with the potential to accelerate snowmelt and disturb the hydrologic cycle [15], also contributing to regional warming [16]. Consequently, and with the concern of climate change effects,

understanding the impact on SSA becomes critical to formulating mitigation strategies for snow-dominated basins.

Several studies have documented the reduction in SSA due to LAPs such as black carbon, brown carbon, and mineral dust and the effects on local hydrological processes [12,13,17–19]. Black carbon (BC), also known as soot [20], is an aerosol generated from the incomplete combustion of fossil fuels, biofuels, and biomass [11,21]. In Asia, BC emissions were found to be a significant precursor of glacier melting in the Himalayas [19], the Tibetan Plateau [22], and regions in Northern China [23]. Brown carbon (BrC) is an organic carbon (OC) fraction, primarily emitted by the incomplete combustion of biomass or by the oxidation of anthropogenic and biogenic gaseous precursors [24]. The effect of BrC is comparable to the snow darkening effect of black carbon, ranging from around half to the same darkening of snow surfaces as soot [25]. Mineral dust is transported to snow-covered areas from arid regions or from anthropogenic sources like opencast mining and the construction industry [26,27]. Events in past years have highlighted the urgency of studying these phenomena in the context of climate change adaptation. Heavy dust loads deposited onto snow surface in the Upper Colorado River Basin [28] or in the European Alps [29] have accelerated snow melt-out, shifting the timing of peak snow-melt-driven runoff and increasing evapotranspiration as vegetation is early exposed. These have consequently altered the basins' hydrological responses. Further, given the relation between climate shifts and natural disasters in high mountain basins [30], these areas are particularly sensitive to disruptions in snowpack dynamics and, therefore, should be closely monitored.

Research along the Chilean central Andes has primarily focused on the reduction of snow albedo by BC [27,31,32]. Since obtaining field measurements in high mountain environments is a difficult task, studies have mainly included point measurements of SSA that do not account for the spatial variability of the complex climatic and topographic conditions of the Chilean Andes [33,34]. The lack of knowledge of the spatial variability of SSA and the distribution of LAPs over the Andes renders albedo estimations for hydrological modelling to empirical parameters, which increases uncertainties in runoff predictions and does not consider the environmental impacts driven by the deposition of these particles. In this context, remote sensing tools emerge as a valuable tool as they provide data at high spatio-temporal resolution for monitoring snow-covered regions at high elevations [35], offering promising opportunities to improve the assessment, observation, and modeling of snow processes [1,36,37].

This study aims to evaluate changes in RF associated with the presence of BC, which is emitted by anthropogenic activities that occur in the Andes, such as vehicular traffic and the mining industry [38]. The solar spectrum was separated into broadband (Bbr) and enclosed (Ecr) ranges to isolate the impact of BC [39]. The broadband range considers wavelengths of 300–2500 nm, while the enclosed range considers a narrower band with wavelengths between 841 and 876 nm. Observations from the Moderate Resolution Imaging Spectroradiometer (MODIS) and modeled ISR from the Chilean Solar Explorer (SE) were used to evaluate temporal and spatial changes in RF, which were validated against in situ SSA and ISR measurements collected in the Upper Aconcagua River Basin (UARB) in the Chilean Central Andes. The MODIS Dust Radiative Forcing in Snow (MODDRFS) [40,41] product was used to estimate the continuous and integrated daily RF for each spectral range, which were analyzed for temporal trends and variability throughout the 2004–2016 period. The paper is organized as follows: Section 2 describes the Materials and Methods and Section 3 presents the Results and Discussion. Finally, the Conclusions are presented in Section 4.

2. Materials and Methods

2.1. Study Area

Central Chile is characterized by a Mediterranean climate, with mild wet winters and dry summers [42]. Precipitation occurs during the austral winter due to sporadic cold fronts, and orographic effects may produce very localized rainfall patterns [43]. Since 2010, the

Central Chile region has experienced a so-called mega-drought, characterized by a series of dry years that typically show a 25% to 45% deficit in annual precipitation [44]. Several studies have reported a significant decrease in snow cover duration and extent [35,45] and significant losses in glacier mass [46] over the last decade.

The study area corresponds to the Upper Aconcagua River Basin (UARB) in the Chilean Central Andes (Figure 1). The watershed is located in the Valparaíso district, approximately 80 km northeast of Santiago, Chile's largest city and capital. The UARB extends between $32^{\circ}15'–33^{\circ}15'$ S and $70^{\circ}0'–70^{\circ}45'$ W, with an area of approximately 3660 km^2 and elevations ranging from 800 to 6000 m above sea level (m.a.s.l.). The mean watershed altitude is approximately 3000 m.a.s.l. The UARB includes four meteorological stations, which are managed by the Dirección General de Aguas de Chile (DGA) and provide daily precipitation and temperature data (Resguardo Los Patos, Riecillos, and Vilcuya) and snow depth data (Portillo, see Figure 1). A laboratory refuge, managed by the Centre for Environmental Technologies (CETAM) of Universidad Técnica Federico Santa María, named NUNATAK-1 (NNTK-1) ($32^{\circ}50'43''$ S, $70^{\circ}07'47''$ W and 3000 m.a.s.l.), measures atmospheric variables such as incident and reflected radiation (shortwave and longwave), air quality (aerosols and gases), and meteorology, including snow depth since 2016. According to data from the meteorological stations, the monthly mean temperature in the UARB typically oscillates between $9.7\text{ }^{\circ}\text{C}$ to $10.9\text{ }^{\circ}\text{C}$ and $19.6\text{ }^{\circ}\text{C}$ to $21.1\text{ }^{\circ}\text{C}$ during the austral winter and summer, respectively, with an annual mean of $15.2\text{ }^{\circ}\text{C}$. However, in the Portillo station, which is close to the location of NNTK-1, the mean annual temperature is $5\text{ }^{\circ}\text{C}$ with temperatures below zero during the winter. The mean annual precipitation is 360 mm, with approximately 280 mm occurring in the fall and winter seasons (May to August). Maximum snow depth occurs in July or August, with values typically exceeding 1700 mm (snow water equivalent of 813 mm) and a historical maximum of 2590 mm in August 1997 (snow water equivalent of 1201 mm) at the Portillo station.

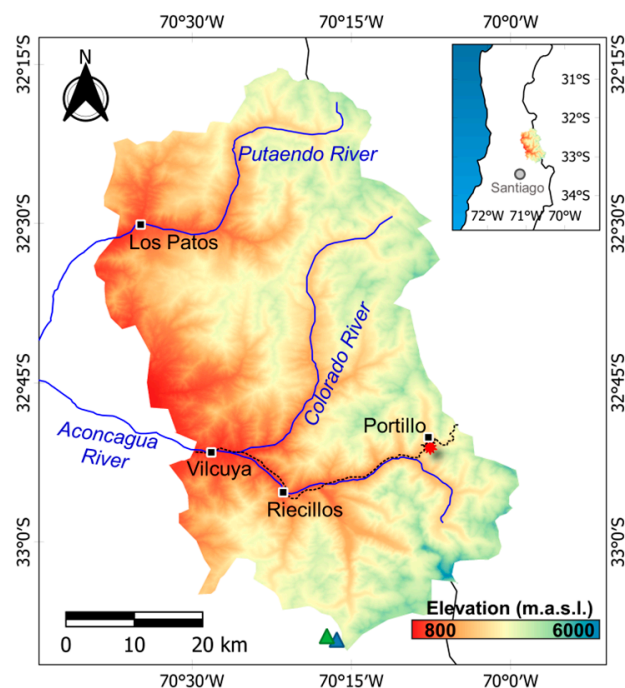


Figure 1. Location of the study area (UARB), indicating the location of meteorological stations, mining activities, and the main traffic route (CH60). Color scale denotes terrain elevation (meters above sea level).

2.2. Database

2.2.1. NUNATAK-1 Laboratory Refuge

NUNATAK-1 (NNTK-1) is a laboratory refuge located at an altitude of 3000 m.a.s.l. (Figure 1) located within the winter quarters of the Mountain School of the Chilean Army in Portillo, a few miles away from the Chile-Argentina border. Its main purpose is to study environmental pollution and atmosphere–cryosphere interactions, specifically how air pollution affects the melting of glaciers and climate change [33,47]. NNTK-1 measures variables such as concentration and size distribution of atmospheric aerosols, atmospheric concentrations of BC and BrC, and net solar irradiance. A portable Kipp & Zonen 4-Component Net Radiometer (CNR4) is used to measure incoming and reflected solar irradiances and estimate surface snow albedo. The radiometer includes a pyranometer, with a sensitivity of 10–20 $\mu\text{VW}^{-1} \text{m}^{-2}$ and a maximum uncertainty of 5% (95% confidence level), which covers the solar spectrum in the 300 to 2800 nm range. The instrument registers the incident and reflected radiation at a 1 min frequency. For this study, only information from the radiometer for the period 2016–2019 was available at the time of data processing. The in situ surface snow albedo ($SSA_{in\ situ}$) was calculated for the 300–2800 nm range as follows:

$$SSA_{in\ situ} = \frac{R_r}{R_i} \quad (1)$$

where R_r and R_i correspond to the reflected and incident radiation, respectively. The ISR and SSA data collected at a frequency of 1 min were aggregated at a daily timescale (only considering daylight hours) with the purpose of comparing them to those obtained from the SE and MODIS. The in situ SSA data were filtered to (i) eliminate data recorded before sunrise and after sunset, (ii) discard spurious measurements caused by sensor obstruction, and (iii) discard data from days with incomplete records.

2.2.2. MODIS Data Processing

The Moderate Resolution Imaging Spectroradiometer (MODIS) is one of the main instruments of the NASA Earth Observing System (EOS) and operates onboard the Terra and Aqua satellites, with records starting in 2000 and extending until the present [48]. The MODIS-Aqua (MYD) and MODIS-Terra (MOD) provide daily and complementary observations of the Earth, passing over the study area approximately at 10 a.m. and 2 p.m. (local time, GMT-3), respectively.

The reflectance data from band 2 (841–876 nm) from the Surface Reflectance Daily L2G Global 500 m SIN Grid, V6 product (M*D09GA), were used to assess the absorption level of incident shortwave radiation (ISR) in the range where the effects of BC are maximized (~880 nm) [39,49]. The SSA in a broadband spectral range for snow (300 to 2500 nm) was obtained from the Snow Cover Daily L3 Global 500 m SIN Grid, V6 product (M*D10A1) [48]. Each data pixel has an indicator for the quality of the measurement (QA), which is used to filter the data. Data were used only if the QA indicated the best quality (QA = 0) or good quality (QA = 1) as a criterion to increase the accuracy of radiative forcing estimations from satellite imagery and reduce the uncertainties in the process [40,41]. For validation purposes, data were extracted from the pixel containing NNTK-1 and compared to the in situ measurements (see Section 2.2.1).

2.2.3. Solar Explorer

The Solar Explorer (SE) (<http://solar.minenergia.cl/exploracion> (accessed on 20 April 2021)) is a tool developed by the Chilean Energy Ministry to calculate the photovoltaic potential in the Chilean territory [50]. The model calculates the shortwave radiation at the top of the atmosphere (RTOA) and at surface level, including ISR and longwave radiation for the 2004 to 2016 period. For these calculations, the model uses the parametrization of solar radiation developed by the Goddard Climate and Radiation Branch (CLIRAD-SW) [51] in combination with information on atmosphere radiation from the TIM/SORCE satellite (Total Irradiance Monitor/Solar Radiation and Climate Experiment) [52], topographic data

from the Shuttle Radar Topography Missions (SRTM) site [53,54], and the Geostationary Operational Environmental Satellite (GOES EAST) [55] for cloud detection. The ISR data have been validated against in situ radiation data from 82 weather stations distributed throughout Chile and provide hourly RTOA and ISR with a spatial resolution of 1 km per pixel (Molina [50]). The ISR data were used in the *RF* calculations after validation against field data from NNTK-1 (see Section 2.2.1).

2.2.4. Validation of SSA and ISR

Snow surface albedo in the broadband range (SSA_{Bbr}) data obtained from M*D10A1 and modeled ISR from the Solar Explorer were validated against in situ SSA and ISR measurements from the NNTK-1 station before estimating the radiative forcing. However, it is worth noting that validation was limited in the temporal range because data were available for different periods at each platform (regarding NNTK-1 measurements). Therefore, validation of MODIS SSA and ISR data could only be conducted for 2016–2019 and 2016, respectively. SSA_{Bbr} from the MODIS-Terra and MODIS-Aqua satellites were compared separately against $SSA_{in\ situ}$, and a correlation analysis was performed on a daily basis for the entire period.

2.3. Radiative Forcing

2.3.1. MODIS Dust Radiative Forcing in Snow (MODDRFS)

The MODDRFS, originally developed by Painter et al. [40] and improved by Miller et al. [41], was used to estimate the radiative forcing (*RF*) over snow. This algorithm was developed to study the *RF* on snowpack resulting from the deposition of mineral dust in the 350–850 nm wavelength range. The instantaneous *RF* is obtained as follows (Miller et al. [41]):

$$RF = \int_{\lambda_0}^{\lambda} F_o(\lambda, t) D(\lambda) d\lambda dt \quad (2)$$

$$F_o(\lambda, t) = F_{dir,local}(\lambda, t) + F_{dif}(\lambda, t) \quad (3)$$

$$F_{dir,local} = F_{dir} \frac{\sin\theta_s * \sin s * \cos(\phi_s - \alpha) + \cos\theta_s \cos s}{\cos\theta_s} \quad (4)$$

$$D(\lambda) = SSA_{fresh} - SSA_{effective} \quad (5)$$

where $F_o(\lambda, t)$ represents the total ISR at a wavelength λ and at time t . The total ISR $F_o(\lambda, t)$ has a local and diffuse direct component (Equation (3)), where $F_{dir,local}(\lambda, t)$ is given by direct radiation $F_{dir}(\lambda, t)$ and diffuse radiation $F_{dif}(\lambda, t)$. Direct radiation is dependent on the conditions at a particular location, such as the angle of solar zenith θ_s , the angle of solar azimuth ϕ_s , slope s , and orientation α of the site (Equation (4)). $D(\lambda)$ corresponds to the difference between the surface snow albedo in ideal conditions, e.g., fresh or pure snow (SSA_{fresh}), and the effective surface snow albedo ($SSA_{effective}$) at a wavelength λ (Equation (5)). The $SSA_{effective}$ was provided by the in situ and satellite measurements, and SSA_{fresh} was estimated using the radiative transfer model SNICAR [56]. The integration limits were defined based on the wavelength range defined for Bbr and Ecr: 300–2500 nm for the M*D10A1 product (Bbr) and 841–876 nm for M*D09GA (Ecr). Finally, the daily integrated *RF* (*DIRF*) from sunrise to sunset is given by:

$$DIRF = \int_{sunrise}^{sunset} \int_{\lambda_0}^{\lambda} F_o(\lambda, t) D(\lambda) d\lambda dt \quad (6)$$

where the terms of this equation have been previously defined in Equations (3) and (5).

2.3.2. Santa Barbara DISORT Atmospheric Radiative Transfer (SBDART)

The Santa Barbara DISORT (Discrete Ordinate Radiative Transfer) Atmospheric Radiative Transfer (SBDART) [57–59] model was used to obtain indirect estimates of the fraction of radiation extracted from the SE that corresponds to the spectral bands provided by the MODIS reflectance products (M*D10A1 and M*D09GA band 2). SBDART models the radiative transfer processes in the atmosphere and Earth's surface (ISR) and requires input such as time, geographic location, atmospheric profile (tropical, mid-latitude, or sub-arctic) in terms of water vapor density and pressure, solar zenith (sza) and azimuth (saza), type of surface albedo, and spectral boundaries. After estimating the total radiation in the 280–4000 nm range using SBDART, the radiation $F_o(\lambda, t)$ that corresponds to the spectral ranges of MODIS products can be obtained. The Ecr and Bbr correspond to approximately 3% and 99% of the total $F_o(\lambda, t)$ extracted from the SE, respectively (see Figure A1). These percentages show small variability throughout the day, which results primarily from changes in solar zenith and azimuth ($\pm 0.3\%$, and $\pm 0.1\%$, respectively). Values obtained at 10 a.m. (MODIS Terra) were determined to be close to the daily mean for both spectral ranges, with differences below 1%.

2.3.3. Snow, Ice, and Aerosol Radiative Model (SNICAR)

The SNICAR [56] is a radiative transfer model developed to simulate spectral snow albedo as a function of snow microstructure, stratigraphy, the concentration of LAPs in snow, and the surface irradiance flux [60]. For this study, SNICAR was used to estimate the fresh and clean snow albedo (SSA_{fresh}), which is required for the calculation of the radiative forcing (Equations (2) and (5)). For the estimation of SSA_{fresh} , clear-sky conditions were assumed, and a snow grain size of 100 μm , which corresponds to a null concentration of pollutants [1,61], and a snow density of 400 kgm^{-3} , which is representative of seasonal snow [62], were used. Optical ice properties were estimated based on the ice refraction index proposed by Picard et al. [63]. An optically semi-infinite and uniform snowpack was considered for the study area [61]. For this purpose, a 0.3 m snowpack depth was assumed, which is enough to reproduce an optically semi-infinite layer for a snowpack with the properties previously described [64–66]. SNICAR albedo simulations showed that SSA_{fresh} is mainly determined by solar position (zenith and azimuth), which varies throughout the austral winter (see Figure A3).

2.3.4. Estimation of SSA, D, and RF at NNTK-1

As described on Equation (6), $D(\lambda)$ is required to estimate the daily integrated radiative forcing (Equation (6)). In turn, the estimation of $D(\lambda)$ requires the SSA and ISR associated with both spectral ranges (Bbr and Ecr). The period of study is defined as between 2004 and 2016, which corresponds to the period where the remote sensing data overlap (MODIS and SE) and, consequently, the daily integrated radiative forcing (DIRF) can be estimated. SSA, D , and DIRF were estimated for all days with clear-sky conditions using the remote sensing data extracted at the location of NNTK-1.

3. Results and Discussion

3.1. Data Validation

MODIS products revealed excessive cloudiness in 2016, such that a comparison against in situ SSA (NNTK-1) measurements was not possible for this year. For the 2017–2019 period, we observed that the percentage of days with clear-sky condition (valid data) in June–July did not exceed 25% of the whole MODIS data set, while for August, this percentage increased to 61%. Comparing the two satellites between June and August, the MOD10A1 product (Terra) presented a larger number of days with clear-sky conditions, as well as a higher monthly correlation value (in the range 0.51–0.91), except for July 2017 and 2018, where the correlation values were lower than 0.13. During June–August, the MYD10A1 product (Aqua) showed correlation values in the range 0.27–0.81; however, lower values were observed for the months of June, July, and October in 2017 (0.02, 0.20,

and 0.21, respectively). The reason for the low correlation values in these months for both satellites may be attributed to two main factors: (i) few days with useful remote sensing data due to excessive cloudiness and (ii) days where the elevation of the snow line (zero isotherm) was relatively close to the elevation of NNTK-1, with the implication of low or partial snow coverage at NNTK-1's pixel (<70%), resulting in an underestimation of more than 10% with respect to the field measurements (see Figure A2). The Solar Explorer data had been previously validated in the study area [50]. Despite this, we computed the correlation between ISR from SE and from NNTK-1, confirming a very high correlation (>0.9) during 2016 (not shown).

3.2. Temporal Analysis of SSA, $D(\lambda)$, and RF during the 2004–2016 Period at NNTK-1

Figure 2 shows SSA values for both spectral ranges (Bbr and Ecr) for the pixel corresponding to NNTK-1. After filtering, 312 days (20% of the study period) with snow and clear-sky conditions were found. SSA exhibits a similar behavior for Bbr (Figure 2a) and the Ecr (Figure 2b), with minimum values during May that increase as the austral winter progresses. The distribution of values until the third quartile is similar for both spectral ranges, ranging between 0.12 and 0.35 in May, 0.25 and 0.67 in June, 0.50 and 0.70 in July, and 0.55 and 0.75 in August. The monthly mean values (shown as white boxes in Figure 2) are similar, with a maximum variation of 0.02 for the month of May.

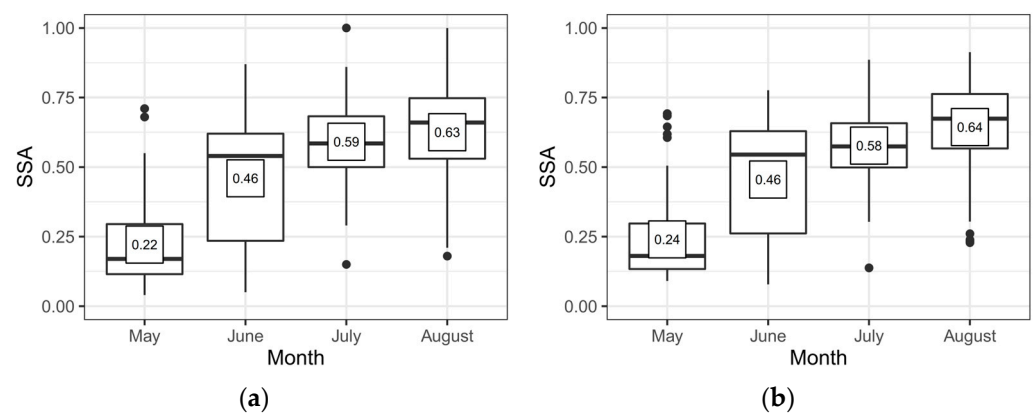


Figure 2. SSA values in the Bbr (a) and Ecr (b), grouped by month in NNTK-1's location, for the 2004–2016 period. The bars represent 50% of the data, with the lower limit being quartile 1, the central limit being quartile 2 or the median, and the upper limit being quartile 3. Black points indicate outliers. The chart also displays the monthly mean value for each month.

To quantify the influence of LAPs on the radiative forcing, the estimation of D (Equation (5)) for both spectral ranges is necessary. D values are obtained using SSA_{fresh} simulated by SNICAR during the austral winter between 2004 and 2016, considering clear-sky and the other conditions outlined in Section 2.3. Daily mean values of 0.863 ± 0.007 for the Bbr and 0.933 ± 0.007 for the Ecr were obtained (see Figure A3). Figure 3 shows estimates of D for the entire study period. For each month, all D_{Ecr} values (Figure 3b) are higher than D_{Bbr} (Figure 3a), including those below quartile 3 and the monthly mean values. D_{Ecr} values within quartile 1 and 3 (above q1 and below q3) are approximately 0.07 units higher for the month of July, whereas for the other months (May, June, and August), values in the Ecr are 0.04 units higher than in the Bbr. The monthly mean values of D (white boxes) in the Ecr are larger by 0.05 units for May and August (during the 2004 to 2016 period) compared to those for Bbr. The monthly mean D_{Ecr} values were also higher than D_{Bbr} for June and July, with differences of 0.07 and 0.08 units, respectively. We note that the differences between D_{Ecr} and D_{Bbr} increase if the analysis is conducted considering the daily mean values. The values of D in the Ecr were generally higher (as much as 0.25 units) than in the Bbr, with the exception of only 60 days within the 2004–2016 period (Figure 4).

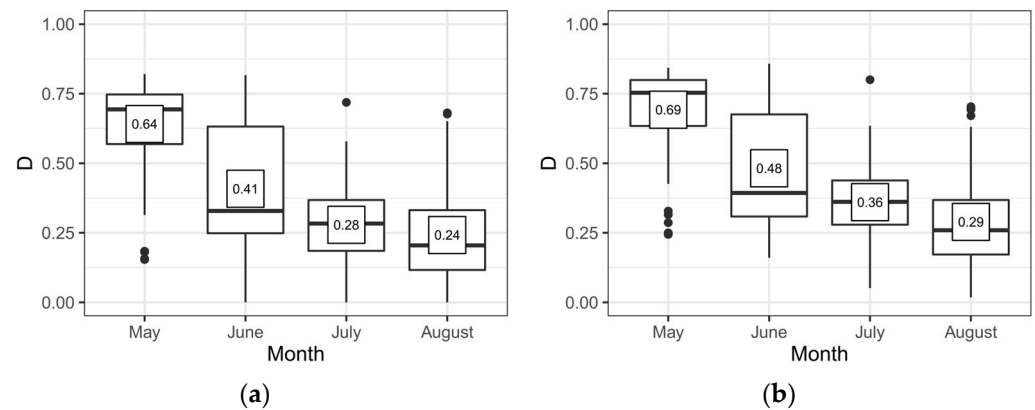


Figure 3. D values in the Bbr (a) and Ecr (b), grouped by month in NNTK-1's location, for the 2004–2016 period. The bars represent 50% of the data, with the lower limit being quartile 1, the central limit being quartile 2 or the median, and the upper limit being quartile 3. Black points indicate outliers. Monthly mean values for each month are included.

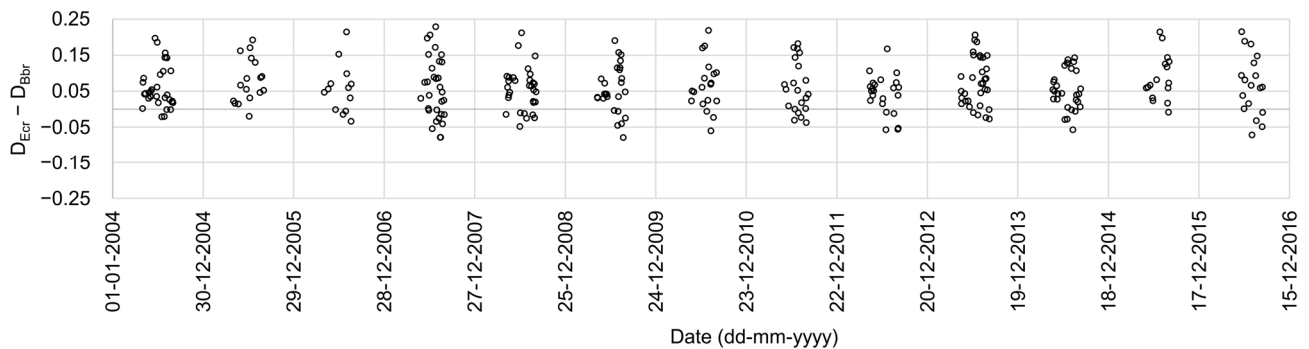


Figure 4. Difference between D in the broadband range (Bbr) and enclosed range (Ecr) for the 2004–2016 period (black circles).

Figure 5 shows the $DIRF$ results for the Bbr and Ecr, which are consistent with the previous results for SSA and D . The $DIRF$ reaches higher monthly mean values (white boxes) in May, with 8.02 and $0.27 \text{ MJ m}^{-2} \text{ d}^{-1}$ for the Bbr and Ecr, respectively, decreasing to 2.82 (Bbr) and $0.12 \text{ MJ m}^{-2} \text{ d}^{-1}$ (Ecr) in July. This scenario follows the trend observed for D between May and July (Figure 3); however, the monthly mean values of the $DIRF$ in August increased to 3.58 (Bbr) and 0.13 (Ecr) $\text{MJ m}^{-2} \text{ d}^{-1}$, whereas D continued to decrease. This difference is explained by the fact that the ISR values reach minimum values during June and July and then start to increase (Figure A4).

In Figure 5, the $DIRF$ values reach $13.21 \text{ MJ m}^{-2} \text{ d}^{-1}$ in the Bbr and $0.42 \text{ MJ m}^{-2} \text{ d}^{-1}$ in the Ecr. These $DIRF_{Ecr}$ values are close to the lower limit of the $DIRF$ values reported by Rowe et al. 2019 at the same location. Although these authors had used a different spectral range to analyze BC effects in snow (650–700 nm), the $DIRF$ values are of the same order of magnitude (0.1 – $2.3 \text{ MJ m}^{-2} \text{ d}^{-1}$). A maximum instantaneous RF in the Bbr of 571.54 W m^{-2} was observed (29 August 2004), which is attributed to the melting of most of the snow at the corresponding pixel (snow cover value of 0.23). The instantaneous radiative forcing found in other regions around the world, such as the Himalaya or across the United States, using the 350–850 nm wavelength range, are comparable with the values obtained here for the Bbr (e.g., [28]).

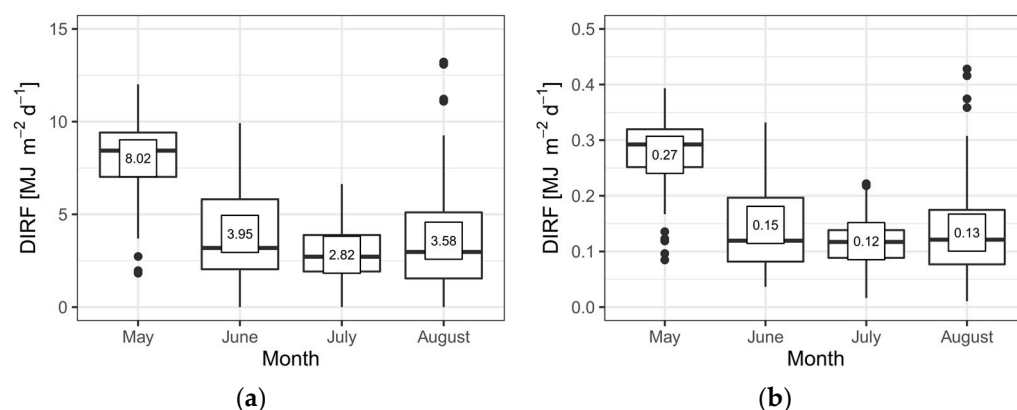


Figure 5. *DIRF* values in the Bbr (a) and Ecr (b), grouped by month in NNTK-1's location, for the 2004–2016 period. The bars represent 50% of the data, with the lower limit being quartile 1, the central limit being quartile 2 or the median, and the upper limit being quartile 3. Black points indicate outliers. Monthly mean values are indicated for each month.

To compare the *DIRF* values between the Ecr and Bbr spectral ranges, which have different magnitudes of received radiation (3% and 99%, as shown in Section 2.3.2), the *DIRF* values were normalized with respect to Bbr. This normalization allows for the determination of the percentage impact on Ecr in terms of the *DIRF* ($DIRF_{Ecr/Bbr}$), which can then be compared to the normalized radiation received in the Ecr ($ISR_{Ecr/Bbr}$). From the monthly mean values in Figure 4, the normalized $DIRF_{Ecr/Bbr}$ values are 3.42%, 3.74%, 4.22%, and 3.74% for the months of May, June, July, and August, respectively. Similarly, the normalized $ISR_{Ecr/Bbr}$ values are 3.17%, 3.22%, 3.23%, and 3.17% for the same months, respectively. As observed, there is a difference between the $ISR_{Ecr/Bbr}$ and $DIRF_{Ecr/Bbr}$ ratios for each of the months evaluated, with higher ratios observed for $DIRF_{Ecr/Bbr}$. This suggests that the variations in SSA in the Ecr are higher and that this increase may be attributed to the presence of LAPs as these particles have a greater impact on the albedo at wavelengths between 841 and 876 nm (Ecr) than in the range of 300–2500 nm (Bbr), regardless of the total amount of received radiation [15,67,68].

With the purpose of following daily changes in SSA, consecutive days without liquid precipitations and with equal or less snow cover after the initial day were selected to make sure that local snowfall at Portillo did not occur (see Table 1). Figure 6 shows the variations in spectral SSA (for MODIS bands 1–4) for the periods that satisfy the former conditions throughout the study period. As expected, the calculations show that SSA decreases with time (from one day to the next) for most cases, which is consistent with the aging of snow and, size increase in snow grains and LAPs deposition, that occur as time progresses after the storm [9,69]. For some of the selected periods, such as 28–29 June 2004 (Figure 6a), 15–16 August 2007 (Figure 6b), 2 July 2016 (Figure 6g), and 6–7 June 2016 (Figure 6m), the spectral SSA values showed an evident decrease in the Ecr (841–876 nm) and the closest MODIS band (620–670 nm), larger than in the 459–479 nm and 545–565 nm bands. However, for the majority of days shown in Figure 6, the decrease in spectral SSA did not show much variation between bands (e.g., Figure 6c–e,h,l,m). Although there was one period where a slight increase in SSA was observed (Figure 6d), these data show a systematic decrease in spectral SSA for the visible wavelengths (MODIS bands 1–4) and particularly for the Ecr, which is usually associated with the presence of BC [19,70]. The fact that the other bands in the visible wavelengths may be associated with the presence of mineral dust [40] is noted.

Table 1. Snow cover (SC), surface snow albedo (SSA), difference between clean and measured SSA (D), and daily integrated radiative forcing ($DIRF$) values for Bbr and Ecr at the NNTK-1. SSA and D values are dimensionless. MODIS bands are organized by smaller to higher wavelength range values: 459–479 nm (band 3), 545–565 nm (band 4), 620–670 nm (band 1), and 841–876 nm (Ecr).

Date	SC [%]	SSA [-]					D [-]		DIRF [$\text{MJ m}^{-2} \text{d}^{-1}$]	
		Bbr	Band 3	Band 4	Band 1	Ecr	Bbr	Ecr	Bbr	Ecr
28 June 2004	82	0.62	0.65	0.68	0.67	0.63	0.25	0.31	2.46	0.10
29 June 2004	80	0.59	0.56	0.55	0.52	0.47	0.28	0.46	2.53	0.14
15 August 2007	70	0.65	0.74	0.76	0.76	0.74	0.21	0.20	3.32	0.10
16 August 2007	68	0.53	0.55	0.52	0.49	0.45	0.33	0.48	5.36	0.25
23 August 2008	85	0.72	0.75	0.78	0.78	0.72	0.14	0.21	2.61	0.12
24 August 2008	84	0.58	0.72	0.74	0.74	0.67	0.28	0.26	5.17	0.15
23 July 2009	76	0.70	0.68	0.69	0.69	0.66	0.17	0.28	2.08	0.11
24 July 2009	69	0.56	0.68	0.69	0.71	0.68	0.31	0.26	4.09	0.11
24 August 2009	84	0.75	0.83	0.85	0.85	0.77	0.11	0.16	0.99	0.04
25 August 2009	81	0.54	0.71	0.72	0.71	0.64	0.32	0.30	5.79	0.17
29 June 2010	80	0.55	0.58	0.59	0.59	0.56	0.32	0.38	3.19	0.12
30 June 2010	74	0.55	0.51	0.51	0.50	0.45	0.32	0.49	3.19	0.16
2 July 2011	79	0.57	0.62	0.62	0.60	0.57	0.30	0.37	2.70	0.11
3 July 2011	76	0.49	0.48	0.45	0.43	0.39	0.38	0.55	3.64	0.17
21 August 2011	76	0.74	0.80	0.82	0.82	0.78	0.12	0.15	2.21	0.09
22 August 2011	72	0.48	0.60	0.61	0.62	0.59	0.38	0.34	7.07	0.20
18 August 2013	85	0.81	0.72	0.79	0.79	0.73	0.05	0.20	0.90	0.11
19 August 2013	82	0.51	0.56	0.58	0.58	0.53	0.35	0.40	6.01	0.22
26 August 2013	75	0.70	0.76	0.78	0.79	0.77	0.16	0.16	3.03	0.09
27 August 2013	69	0.42	0.50	0.51	0.53	0.52	0.44	0.41	8.31	0.24
23 July 2014	77	0.58	0.55	0.57	0.56	0.54	0.29	0.40	3.21	0.14
24 July 2014	74	0.42	0.47	0.49	0.51	0.49	0.45	0.45	5.27	0.17
16 August 2015	83	0.73	0.82	0.81	0.81	0.74	0.13	0.19	2.19	0.10
17 August 2015	78	0.53	0.67	0.67	0.66	0.61	0.33	0.32	5.73	0.17
6 June 2016	75	0.80	0.83	0.83	0.83	0.78	0.07	0.16	0.69	0.05
7 June 2016	76	0.76	0.72	0.70	0.67	0.61	0.11	0.32	1.11	0.11
29 August 2016	75	0.54	0.55	0.58	0.58	0.55	0.32	0.38	6.24	0.23
30 August 2016	75	0.32	0.38	0.41	0.43	0.40	0.54	0.53	7.42	0.23

Table 1 shows daily SSA variations for MODIS bands 1, 3, and 4 and for the Bbr and Ecr spectral ranges, as well as daily D and $DIRF$ values for the Bbr and Ecr. Differences in SSA for bands 1, 3, 4, and Ecr until -0.3 are observed, with a larger difference observed for the second day (see Figure 6). The maximum daily rates of albedo decrease for the Bbr and Ecr were observed in August 2013 and August 2007, respectively. These reductions in albedo seem to be much higher than the values reported by previous studies in the Central Andes area [33–35]. Cereceda-Balic et al. 2018 reported a reduction of 0.08 units per day in the broadband albedo (SSA_{Bbr}), resulting from the deposition of BC from vehicle emissions in the Portillo location. These differences are attributed to (i) differences in the magnitude of the contamination sources associated with the periods and locations considered in the studies and (ii) the fact that the remote sensing measurements consist of only one measurement, either at 10 a.m. or 2 p.m., whereas the in situ study used continuous data from a radiometer [33].

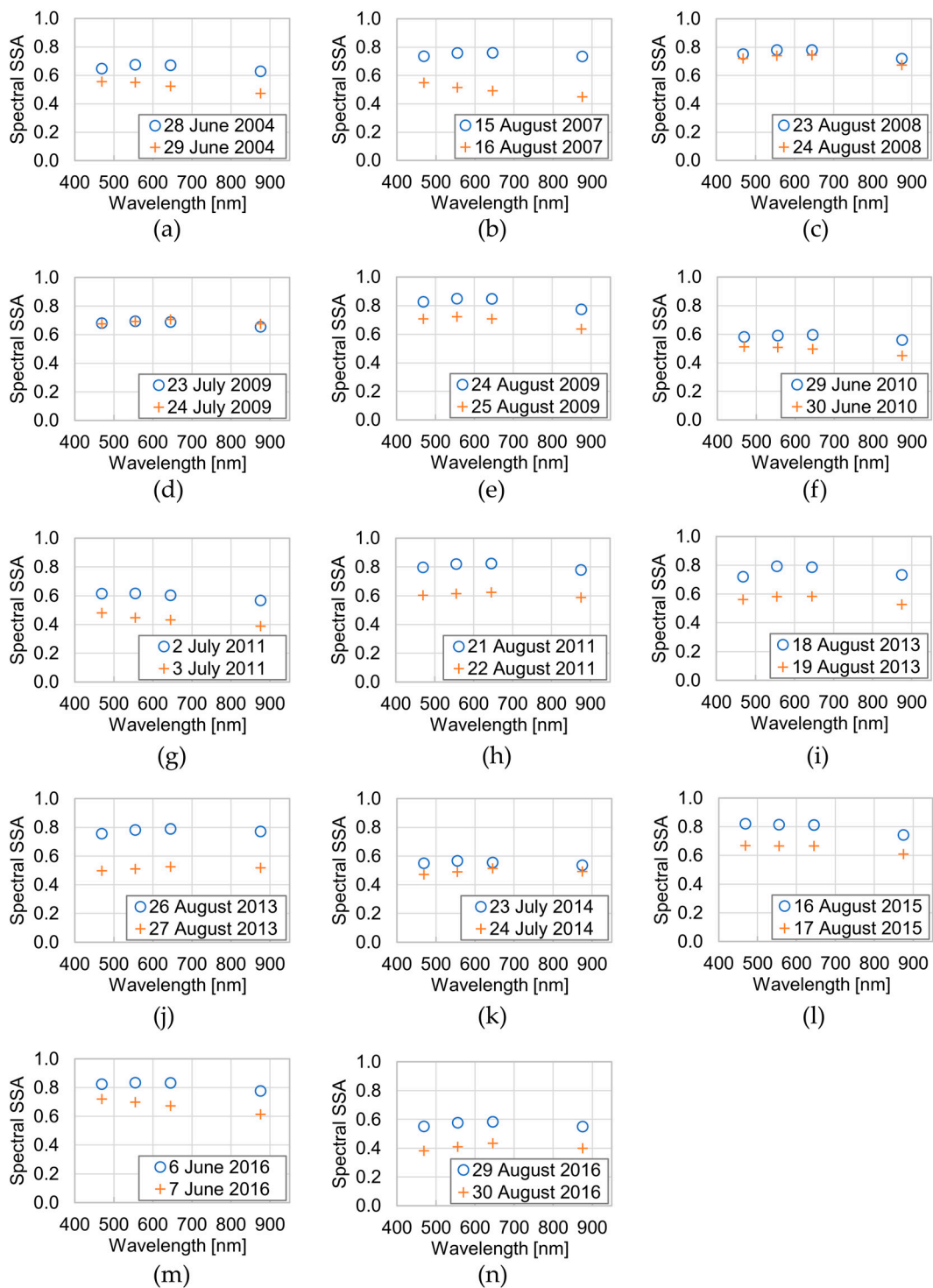


Figure 6. SSA spectral variations for MODIS bands (1–4) for 14 days of the study period are displayed in sub-figures (a–n). Blue circles and orange crosses represent consecutive days.

The results presented in Table 1 also show the differences in daily integrated radiative forcing ($DIRF$) for the two spectral ranges of interest (Ecr and Bbr) for two consecutive days. On the second day, the $DIRF_{Bbr}$ shows a 60% increase compared with the average radiative forcing of the evaluated days, whereas the $DIRF_{Ecr}$ exhibited an increase of approximately 50%. When examining the $DIRF_{Ecr/Bbr}$, the radiative forcing in the Ecr band represents on average 4.46% of the radiative forcing in the Bbr, with a maximum value of 12.21% (18 August 2013). On the other hand, the incident solar radiation ratio $ISR_{Ecr/Bbr}$ is on

average 3.18% for the days considered in Table 1, with maximum values that reach 3.21% for 6–7 June 2016 and 3.14% for 18 August 2013. The above confirms previous results indicating that radiative forcing has a greater percentage impact on the narrow Ecr band than on the much broader Bbr.

4. Conclusions

The main objective of this study was to assess the changes in the radiative forcing associated with the presence of BC in a snow-covered region within the Chilean Central Andes. The central contributions of this paper arise from the data and model employed to estimate the changes in radiative forcing. First, high-quality in situ data from the NUNATAK-1 platform were used to validate the remote sensing MODIS SSA estimates and to calculate the radiative forcing. The NUNATAK-1 laboratory stands as one of the two facilities in the Chilean Central Andes equipped for the continuous monitoring of SSA and other environmental parameters that enable the study of snowmelt dynamics. The analyses show that the MOD10A1 product serves as a dependable source for obtaining SSA in the remote and frequently inaccessible area of the Central Andes from which radiative forcing estimates can be derived. Second, the MODDRFS model, originally developed by Painter et al. [40], evaluates the changes in radiative forcing using only the 350–876 nm spectral range. In this paper, the spectral range used to estimate the radiative forcing is extended to the 300–2500 nm range (Bbr) to include SSA data from remote sensing, in situ, and model (SNICAR) sources, with spectral ranges that do not match the original range developed by Painter et al. (2012). The 841–876 nm spectral range is evaluated to isolate the effects of BC on SSA, which is known to be a key factor influencing SSA variability in the study area.

The higher sensitivity of SSA in the Ecr (than in the Bbr) suggests that BC particles (and probably other LAPs) are present in the Andean snowpack, impacting snowpack radiation reflection. Overall, we found that the reductions in albedo are generally higher than those reported by previous studies in the area using in situ characterizations, which we attribute to differences in the magnitude of the atmospheric contamination that may exist in the different time periods used in the studies and the temporal resolution of the remote sensing data. Nonetheless, the remote sensing MODIS data proved to be a valuable tool for estimating the radiative forcing in regions that are typically inaccessible and improving our understanding of the variability in SSA, which is essential to accurately predict snowmelt and glacier retreat, which in turn control river discharge and freshwater availability in mountain regions.

Author Contributions: Conceptualization, L.F.-V., L.C., R.P.F., T.R.B.-O. and F.C.-B.; methodology, L.F.-V., L.C., R.P.F., T.R.B.-O. and D.P.-F.; software, L.F.-V., T.R.B.-O. and D.P.-F.; validation, L.F.-V., T.R.B.-O. and D.P.-F.; formal analysis, L.F.-V., L.C., R.P.F., T.R.B.-O. and D.P.-F.; investigation, L.F.-V., L.C., R.P.F., T.R.B.-O., D.P.-F. and F.C.-B.; resources, L.C., R.P.F., T.R.B.-O. and F.C.-B.; data curation, L.F.-V., T.R.B.-O. and D.P.-F.; writing—original draft preparation, L.F.-V., L.C., R.P.F., T.R.B.-O. and D.P.-F.; visualization, L.F.-V., T.R.B.-O. and D.P.-F.; supervision, L.C., R.P.F., T.R.B.-O. and F.C.-B.; funding acquisition, L.C., R.P.F., T.R.B.-O. and F.C.-B. All authors have read and agreed to the published version of the manuscript.

Funding: This research was funded by the National Research and Development Agency of Chile (ANID), namely, the ANID-ANILLO ACT210021, ANID-FONDECYT REGULAR 1221526, ANID-FONDECYT 11220482, ANID-FONDECYT 1231494, and ANID-FONDECYT 3230555 projects and the Centre for Environmental Technologies-Universidad Técnica Federico Santa María (CETAM-UTFSM).

Data Availability Statement: Data provided on request.

Acknowledgments: We would like to thank the MODIS-NASA, Solar Explorer (Explorador Solar), and NUNATAK-1 laboratory refuge (CETAM-USM) scientific teams and their associated personnel for the production of the data used in this research effort.

Conflicts of Interest: The authors declare no conflict of interest.

Abbreviations

BC	Black carbon
Bbr	Broadband range
CETAM	Centre for Environmental Technologies
D	Difference between SSA_{fresh} and $SSA_{\text{effective}}$
D_{Bbr}	D in the broadband range
D_{Ecr}	D in the enclosed range
DIRF	Daily integrated radiative forcing
$DIRF_{\text{Bbr}}$	DIRF in the broadband range
$DIRF_{\text{Ecr}}$	DIRF in the enclosed range
Ecr	Enclosed range
ISR	Incident shortwave radiation
LAPs	Light-absorbing particles
MODIS	Moderate Resolution Imaging Spectroradiometer
M*D10A1	Refers to both MOD10A1 and MYD10A1, remote sensing products used to estimate SSA_{Bbr}
M*D09GA	Refers to both MOD09GA and MYD09GA, remote sensing products used to estimate SSA_{Ecr}
NUNATAK-1	Refuge laboratory operated by CETAM
RF	Radiative Forcing due to SSA decreasing
SE	Solar Explorer
SSA	Surface snow albedo
SSA_{Bbr}	SSA in the broadband range
SSA_{fresh}	SSA in fresh condition (pure and clean)
$SSA_{\text{effective}}$	SSA effective estimated with M*D10A1 and M*D09GA
$SSA_{\text{in situ}}$	SSA measured in situ by NUNATAK-1
UARB	Upper Aconcagua River Basin

Appendix A

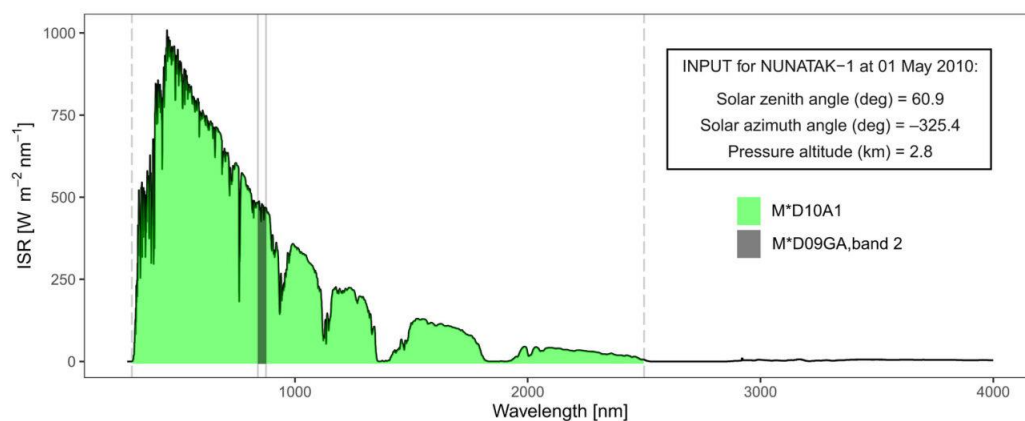


Figure A1. Example of spectral incident shortwave radiation (ISR) on the surface in the shortwave range model through SBDART for NNTK-1 at 10:00 a.m. of 5 May 2010. Black line represents the Solar Explorer ISR spectral range (up to the 4000 nm wavelength). In green, the spectral range for M*D10A1 (Bbr), and in gray, the spectral range for M*D09GA band 2 (Ecr). The radiation for Bbr and Ecr are equivalent to 99% and 3%, respectively, with regard to Solar Explorer radiation.

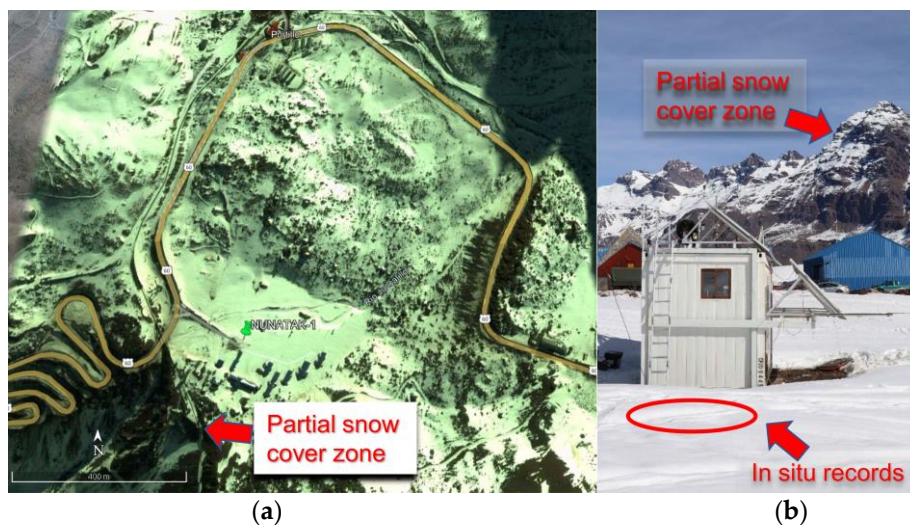


Figure A2. Layout of (a) MODIS pixel where NNTK-1 is located. Also, shows image of (b) specific place where records were taken and around NNTK-1.

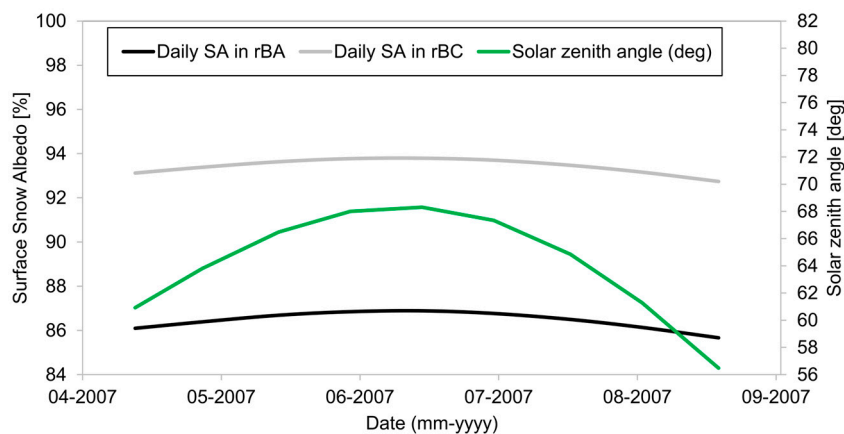


Figure A3. Daily SSA_{fresh} values simulated with SNICAR at 10 a.m. in the Bbr (black line) and Ecr (gray line), in function of the sza (green line) in NNTK-1, for the months of May to August 2007. Other years have a variation of 1.5 sza degrees, which indicates a variation of ± 0.001 (included in the uncertainties mentioned in Section 3.2) in the SSA for Bbr and Ecr.

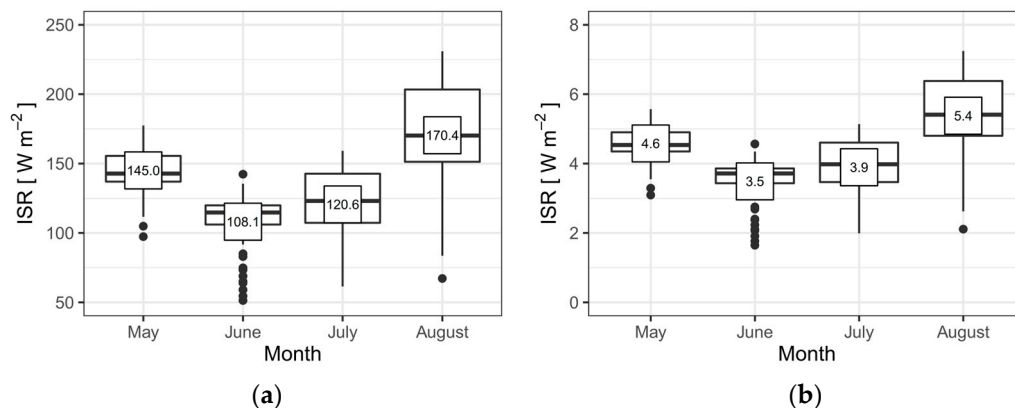


Figure A4. Incident shortwave radiation (ISR) in the Bbr (a) and Ecr (b), grouped by month, for the 2004–2016 period. The bars represent 50% of the data, with the lower limit being quartile 1, the central limit being quartile 2 or the median, and the upper limit being quartile 3. Black points indicate outliers. Monthly mean values are shown for each month.

References

1. Beres, N.D.; Lapuerta, M.; Cereceda-Balic, F.; Moosmüller, H. Snow Surface Albedo Sensitivity to Black Carbon: Radiative Transfer Modelling. *Atmosphere* **2020**, *11*, 1077. [[CrossRef](#)]
2. Barry, R.G.; Armstrong, R.; Callaghan, T.; Cherry, J.; Gearheard, S.; Nolin, A.; Russell, D.; Zöcler, C. *Global Outlook for Ice & Snow*; UNEP: Nairobi, Kenya, 2007.
3. IPCC. *Climate Change 2007: Impacts, Adaptation and Vulnerability: Contribution of Working Group II to the Fourth Assessment Report of the Intergovernmental Panel*; IPCC: Geneva, Switzerland, 2007.
4. IPCC. *Climate Change 2013: The Physical Science Basis. Contribution of Working Group I to the Fifth Assessment Report of the Intergovernmental Panel on Climate Change*; Cambridge University Press: Cambridge, UK; New York, NY, USA, 2013; p. 1535.
5. Xu, L.; Dirmeyer, P. Snow—Atmosphere Coupling Strength. Part II: Albedo Effect Versus Hydrological Effect. *J. Hydrometeorol.* **2013**, *14*, 404–418. [[CrossRef](#)]
6. Gardner, A.S.; Sharp, M.J. A Review of Snow and Ice Albedo and the Development of a New Physically Based Broadband Albedo Parameterization. *J. Geophys. Res. Earth Surf.* **2010**, *115*, F01009. [[CrossRef](#)]
7. Beres, N.D.; Sengupta, D.; Samburova, V.; Khlystov, A.Y.; Moosmüller, H. Deposition of Brown Carbon onto Snow: Changes in Snow Optical and Radiative Properties. *Atmos. Chem. Phys.* **2020**, *20*, 6095–6114. [[CrossRef](#)]
8. Warren, S.G.; Wiscombe, W.J. A Model for the Spectral Albedo of Snow. II: Snow Containing Atmospheric Aerosols. *J. Atmos. Sci.* **1980**, *37*, 2734–2745. [[CrossRef](#)]
9. Hadley, O.L.; Kirchstetter, T.W. Black-Carbon Reduction of Snow Albedo. *Nat. Clim. Chang.* **2012**, *2*, 437–440. [[CrossRef](#)]
10. He, C.; Takano, Y.; Liou, K.N.; Yang, P.; Li, Q.; Chen, F. Impact of Snow Grain Shape and Black Carbon-Snow Internal Mixing on Snow Optical Properties: Parameterizations for Climate Models. *J. Clim.* **2017**, *30*, 10019–10036. [[CrossRef](#)]
11. Bond, T.C.; Doherty, S.J.; Fahey, D.W.; Forster, P.M.; Berntsen, T.; DeAngelo, B.J.; Flanner, M.G.; Ghan, S.; Kärcher, B.; Koch, D.; et al. Bounding the Role of Black Carbon in the Climate System: A Scientific Assessment. *J. Geophys. Res. Atmos.* **2013**, *118*, 5380–5552. [[CrossRef](#)]
12. Skiles, S.M.K.; Painter, T. Daily Evolution in Dust and Black Carbon Content, Snow Grain Size, and Snow Albedo during Snowmelt, Rocky Mountains, Colorado. *J. Glaciol.* **2017**, *63*, 118–132. [[CrossRef](#)]
13. Painter, T.H.; Skiles, S.M.; Deems, J.S.; Bryant, A.C.; Landry, C.C. Dust Radiative Forcing in Snow of the Upper Colorado River Basin: 1. A 6 Year Record of Energy Balance, Radiation, and Dust Concentrations. *Water Resour. Res.* **2012**, *48*, W07521. [[CrossRef](#)]
14. Dang, C.; Warren, S.G.; Fu, Q.; Doherty, S.J.; Sturm, M.; Su, J. Measurements of Light-Absorbing Particles in Snow across the Arctic, North America, and China: Effects on Surface Albedo. *J. Geophys. Res. Atmos.* **2017**, *122*, 10149–10168. [[CrossRef](#)]
15. Skiles, S.M.K.; Flanner, M.; Cook, J.M.; Dumont, M.; Painter, T.H. Radiative Forcing by Light-Absorbing Particles in Snow. *Nat. Clim. Chang.* **2018**, *8*, 964–971. [[CrossRef](#)]
16. Hansen, J.; Nazarenko, L. Soot Climate Forcing via Snow and Ice Albedos. *Proc. Natl. Acad. Sci. USA* **2004**, *101*, 423–428. [[CrossRef](#)] [[PubMed](#)]
17. Bryant, A.; Painter, T.H.; Deems, J.; Bender, S.M. Hydrologic Response to Dust Radiative Forcing in Snow in the Upper Colorado River Basin. *Geophys. Res. Lett.* **2013**, *40*, 3945–3949. [[CrossRef](#)]
18. Jacobi, H.W.; Lim, S.; Ménégos, M.; Ginot, P.; Laj, P.; Bonasoni, P.; Stocchi, P.; Marinoni, A.; Arnaud, Y. Black Carbon in Snow in the Upper Himalayan Khumbu Valley, Nepal: Observations and Modeling of the Impact on Snow Albedo, Melting, and Radiative Forcing. *Cryosphere* **2015**, *9*, 1685–1699. [[CrossRef](#)]
19. Santra, S.; Verma, S.; Fujita, K.; Chakraborty, I.; Boucher, O.; Takemura, T.; Burkhart, J.F.; Matt, F.; Sharma, M. Simulations of Black Carbon (BC) Aerosol Impact over Hindu Kush Himalayan Sites: Validation, Sources, and Implications on Glacier Runoff. *Atmos. Chem. Phys.* **2019**, *19*, 2441–2460. [[CrossRef](#)]
20. Petzold, A.; Ogren, J.A.; Fiebig, M.; Laj, P.; Li, S.M.; Baltensperger, U.; Holzer-Popp, T.; Kinne, S.; Pappalardo, G.; Sugimoto, N.; et al. Recommendations for Reporting Black Carbon Measurements. *Atmos. Chem. Phys.* **2013**, *13*, 8365–8379. [[CrossRef](#)]
21. Lapuerta, M.; González-Correa, S.; Ballesteros, R.; Cereceda-Balic, F.; Moosmüller, H. Albedo Reduction for Snow Surfaces Contaminated with Soot Aerosols: Comparison of Experimental Results and Models. *Aerosol Sci. Technol.* **2022**, *56*, 847–858. [[CrossRef](#)]
22. Lee, W.L.; Liou, K.N.; He, C.; Liang, H.C.; Wang, T.C.; Li, Q.; Liu, Z.; Yue, Q. Impact of Absorbing Aerosol Deposition on Snow Albedo Reduction over the Southern Tibetan Plateau Based on Satellite Observations. *Theor. Appl. Climatol.* **2017**, *129*, 1373–1382. [[CrossRef](#)]
23. Zhong, X.; Kang, S.; Zhang, W.; Yang, J.; Li, X.; Zhang, Y.; Liu, Y.; Chen, P. Light-Absorbing Impurities in Snow Cover across Northern Xinjiang, China. *J. Glaciol.* **2019**, *65*, 940–956. [[CrossRef](#)]
24. Saleh, R.; Robinson, E.S.; Tkacik, D.S.; Ahern, A.T.; Liu, S.; Aiken, A.C.; Sullivan, R.C.; Presto, A.A.; Dubey, M.K.; Yokelson, R.J.; et al. Brownness of Organics in Aerosols from Biomass Burning Linked to Their Black Carbon Content. *Nat. Geosci.* **2014**, *7*, 647–650. [[CrossRef](#)]
25. Brown, H.; Wang, H.; Flanner, M.; Liu, X.; Singh, B.; Zhang, R.; Yang, Y.; Wu, M. Brown Carbon Fuel and Emission Source Attributions to Global Snow Darkening Effect. *J. Adv. Model. Earth Syst.* **2022**, *14*, e2021MS002768. [[CrossRef](#)]
26. Moosmüller, H.; Chakraborty, R.K.; Arnott, W.P. Aerosol Light Absorption and Its Measurement: A Review. *J. Quant. Spectrosc. Radiat. Transf.* **2009**, *110*, 844–878. [[CrossRef](#)]

27. Cereceda-Balic, F.; Ruggeri, M.F.; Vidal, V.; Ruiz, L.; Fu, J.S. Understanding the Role of Anthropogenic Emissions in Glaciers Retreat in the Central Andes of Chile. *Environ. Res.* **2022**, *214*, 113756. [[CrossRef](#)] [[PubMed](#)]
28. Painter, T.H.; Deems, J.S.; Belnap, J.; Hamlet, A.F.; Landry, C.C.; Udall, B. Response of Colorado River Runoff to Dust Radiative Forcing in Snow. *Proc. Natl. Acad. Sci. USA* **2010**, *107*, 17125–17130. [[CrossRef](#)] [[PubMed](#)]
29. Di Mauro, B.; Garzonio, R.; Rossini, M.; Filippa, G.; Pogliotti, P.; Galvagno, M.; Morra Di Cella, U.; Migliavacca, M.; Baccolo, G.; Clemenza, M.; et al. Saharan Dust Events in the European Alps: Role in Snowmelt and Geochemical Characterization. *Cryosphere* **2019**, *13*, 1147–1165. [[CrossRef](#)]
30. Shugar, D.H.; Jacquemart, M.; Shean, D.; Bhurushan, S.; Upadhyay, K.; Sattar, A.; Schwanghart, W.; McBride, S.; de Vires, M.V.W.; Mergili, M.; et al. A Massive Rock and Ice Avalanche Caused the 2021 Disaster at Chamoli, Indian Himalaya. *Science* **2021**, *373*, 300–373. [[CrossRef](#)]
31. Bolaño-Ortiz, T.R.; Pascual-Flores, R.M.; López-Noreña, A.I.; Ruggeri, M.F.; Lakkis, S.G.; Fernández, R.P.; Puliafito, S.E. Assessment of Absorbing Aerosols on Austral Spring Snow Albedo Reduction by Several Basins in the Central Andes of Chile from Daily Satellite Observations (2000–2016) and a Case Study with the WRF-Chem Model. *SN Appl. Sci.* **2019**, *1*, 1352. [[CrossRef](#)]
32. Cordero, R.R.; Sepúlveda, E.; Feron, S.; Wang, C.; Damiani, A.; Fernandez, F.; Neshyba, S.; Rowe, P.M.; Asencio, V.; Carrasco, J.; et al. Black Carbon in the Southern Andean Snowpack. *Environ. Res. Lett.* **2022**, *17*, 044042. [[CrossRef](#)]
33. Cereceda-Balic, F.; Vidal, V.; Moosmüller, H.; Lapuerta, M. Reduction of Snow Albedo from Vehicle Emissions at Portillo, Chile. *Cold Reg. Sci. Technol.* **2018**, *146*, 43–52. [[CrossRef](#)]
34. Rowe, P.M.; Cordero, R.R.; Warren, S.G.; Stewart, E.; Doherty, S.J.; Pankow, A.; Schrempf, M.; Casassa, G.; Carrasco, J.; Pizarro, J.; et al. Black Carbon and Other Light-Absorbing Impurities in Snow in the Chilean Andes. *Sci. Rep.* **2019**, *9*, 4008. [[CrossRef](#)] [[PubMed](#)]
35. Malmros, J.K.; Mernild, S.H.; Wilson, R.; Tagesson, T.; Fensholt, R. Snow Cover and Snow Albedo Changes in the Central Andes of Chile and Argentina from Daily MODIS Observations (2000–2016). *Remote Sens. Environ.* **2018**, *209*, 240–252. [[CrossRef](#)]
36. Pu, W.; Cui, J.; Shi, T.; Zhang, X.; He, C.; Wang, X. The Remote Sensing of Radiative Forcing by Light-Absorbing Particles (LAPs) in Seasonal Snow over Northeastern China. *Atmos. Chem. Phys.* **2019**, *19*, 9949–9968. [[CrossRef](#)]
37. Dowson, A.J.; Sirguey, P.; Cullen, N.J. Variability in Glacier Albedo and Links to Annual Mass Balance for the Gardens of Eden and Allah, Southern Alps, New Zealand. *Cryosphere* **2020**, *14*, 3425–3448. [[CrossRef](#)]
38. Molina, L.T.; Andrade, M.; Baumgardner, D.; Casassa, G.; Dawidowski, L.; Garreaud, R.; Huneus, N.; Lambert, F. Pollution and Its Impacts on the South American Cryosphere. *Earth's Futur.* **2015**, *3*, 345–369. [[CrossRef](#)]
39. Sharma, S.; Richard Leitch, W.; Huang, L.; Veber, D.; Kolonjari, F.; Zhang, W.; Hanna, S.J.; Bertram, A.K.; Ogren, J.A. An Evaluation of Three Methods for Measuring Black Carbon in Alert, Canada. *Atmos. Chem. Phys.* **2017**, *17*, 15225–15243. [[CrossRef](#)]
40. Painter, T.H.; Bryant, A.C.; Skiles, S.M. Radiative Forcing by Light Absorbing Impurities in Snow from MODIS Surface Reflectance Data. *Geophys. Res. Lett.* **2012**, *39*. [[CrossRef](#)]
41. Miller, S.D.; Wang, F.; Burgess, A.B.; McKenzie Skiles, S.; Rogers, M.; Painter, T.H. Satellite-Based Estimation of Temporally Resolved Dust Radiative Forcing in Snow Cover. *J. Hydrometeorol.* **2016**, *17*, 1999–2011. [[CrossRef](#)]
42. Bown, F.; Rivera, A.; Acuña, C. Recent Glacier Variations at the Aconcagua Basin, Central Chilean Andes. *Ann. Glaciol.* **2008**, *48*, 43–48. [[CrossRef](#)]
43. Falvey, M.; Garreaud, R.D. Wintertime Precipitation Episodes in Central Chile: Associated Meteorological Conditions and Orographic Influences. *J. Hydrometeorol.* **2007**, *8*, 171–193. [[CrossRef](#)]
44. Garreaud, R.D.; Boisier, J.P.; Rondanelli, R.; Montecinos, A.; Veloso-aguila, H.H.S.D. The Central Chile Mega Drought (2010–2018): A Climate Dynamics Perspective. *Int. J. Clim.* **2020**, *40*, 421–439. [[CrossRef](#)]
45. Saavedra, F.A.; Kampf, S.K.; Fassnacht, S.R.; Sibold, J.S. Changes in Andes Snow Cover from MODIS Data, 2000–2016. *Cryosphere* **2018**, *12*, 1027–1046. [[CrossRef](#)]
46. Dussaillant, I.; Berthier, E.; Brun, F.; Masiokas, M.; Hugonnet, R.; Favier, V.; Rabatel, A.; Pitte, P.; Ruiz, L. Two Decades of Glacier Mass Loss along the Andes. *Nat. Geosci.* **2019**, *12*, 802–808. [[CrossRef](#)]
47. Cereceda-Balic, F.; Vidal, V.; Moosmüller, H. Long-Time Atmospheric Monitoring Data, Snow Albedo and BC in Snow Measured in Portillo, Los Andes Mountains, Chile. In Proceedings of the Air & Waste Management Association's 112th Conference & Exhibition (ACE 2019), Quebec City, QC, Canada, 25–28 June 2019.
48. Hall, D.K.; Riggs, G.A.; Salomonson, V.V.; DiGirolamo, N.E.; Bayr, K.J. MODIS Snow-Cover Products. *Remote Sens. Environ.* **2002**, *83*, 181–194. [[CrossRef](#)]
49. Jing, J.; Wu, Y.; Tao, J.; Che, H.; Xia, X.; Zhang, X.; Yan, P.; Zhao, D.; Zhang, L. Observation and Analysis of Near-Surface Atmospheric Aerosol Optical Properties in Urban Beijing. *Particuology* **2015**, *18*, 144–154. [[CrossRef](#)]
50. Molina, A.; Falvey, M.; Rondanelli, R. A Solar Radiation Database for Chile. *Sci. Rep.* **2017**, *7*, 14823. [[CrossRef](#)]
51. Chou, M.-D.; Suarez, M. A Solar Radiation Parameterization (CLIRAD-SW) for Atmospheric Studies. *NASA Tech. Memo* **1999**, *40*, 10460.
52. Kopp, G.; Lawrence, G.; Rottman, G. The Total Irradiance Monitor (TIM): Science Results. *Sol. Phys.* **2005**, *230*, 129–139. [[CrossRef](#)]
53. Van Zyl, J.J. The Shuttle Radar Topography Mission (SRTM): A Breakthrough in Remote Sensing of Topography. *Acta Astronaut.* **2001**, *48*, 559–565. [[CrossRef](#)]
54. Mukul, M.; Srivastava, V.; Jade, S.; Mukul, M. Uncertainties in the Shuttle Radar Topography Mission (SRTM) Heights: Insights from the Indian Himalaya and Peninsula. *Sci. Rep.* **2017**, *7*, 41672. [[CrossRef](#)]

55. Hillger, D.W.; Schmit, T.J. Observing Systems: The GOES-13 Science Test: A Synopsis. *Bull. Am. Meteorol. Soc.* **2009**, *90*, 592–597. [[CrossRef](#)]
56. Flanner, M.G.; Arnheim, J.B.; Cook, J.M.; Dang, C.; He, C.; Huang, X.; Singh, D.; Skiles, S.M.; Whicker, C.A.; Zender, C.S. SNICAR-ADv3: A Community Tool for Modeling Spectral Snow Albedo. *Geosci. Model Dev.* **2021**, *14*, 7673–7704. [[CrossRef](#)]
57. Ricchiuzzi, P.; Yang, S.; Gautier, C.; Sowle, D. SBDART: A Research and Teaching Software Tool for Plane-Parallel Radiative Transfer in the Earth's Atmosphere. *Bull. Am. Meteorol. Soc.* **1998**, *79*, 2101–2114. [[CrossRef](#)]
58. Obregón, M.A.; Serrano, A.; Costa, M.J.; Silva, A.M. Validation of LibRadtran and SBDART Models under Different Aerosol Conditions. *IOP Conf. Ser. Earth Environ. Sci.* **2015**, *28*, 012010. [[CrossRef](#)]
59. Fu, Y.; Zhu, J.; Yang, Y.; Yuan, R.; Liu, G.; Xian, T.; Liu, P. Grid-Cell Aerosol Direct Shortwave Radiative Forcing Calculated Using the SBDART Model with MODIS and AERONET Observations: An Application in Winter and Summer in Eastern China. *Adv. Atmos. Sci.* **2017**, *34*, 952–964. [[CrossRef](#)]
60. Flanner, M.G.; Zender, C.S.; Randerson, J.T.; Rasch, P.J. Present-Day Climate Forcing and Response from Black Carbon in Snow. *J. Geophys. Res.* **2007**, *112*, D11202. [[CrossRef](#)]
61. Dang, C.; Fu, Q.; Warren, S.G. Effect of Snow Grain Shape on Snow Albedo. *J. Atmos. Sci.* **2016**, *73*, 3573–3583. [[CrossRef](#)]
62. Cornwell, E.; Molotch, N.P.; McPhee, J. Spatio-Temporal Variability of Snow Water Equivalent in the Extra-Tropical Andes Cordillera from Distributed Energy Balance Modeling and Remotely Sensed Snow Cover. *Hydrol. Earth Syst. Sci.* **2016**, *20*, 411–430. [[CrossRef](#)]
63. Picard, G.; Libois, Q.; Arnaud, L. Refinement of the Ice Absorption Spectrum in the Visible Using Radiance Profile Measurements in Antarctic Snow. *Cryosphere* **2016**, *10*, 2655–2672. [[CrossRef](#)]
64. Chen, A.; Li, W.; Li, W.; Liu, X. An observational study of snow aging and the seasonal variation of snow albedo by using data from Col de Porte, France. *Chin. Sci. Bull.* **2014**, *59*, 4881–4889. [[CrossRef](#)]
65. Zhou, X.; Li, S.; Stamnes, K. Effects of vertical inhomogeneity on snow spectral albedo and its implication for optical remote sensing of snow. *J. Geophys. Res.* **2003**, *108*, 4738. [[CrossRef](#)]
66. Wiscombe, W.J.; Warren, S.G. A Model for the Spectral Albedo of Snow. I: Pure Snow. *J. Atmos. Sci.* **1980**, *37*, 2712–2733. [[CrossRef](#)]
67. Cereceda-Balic, F.; Vidal, V.; Ruggeri, M.F.; González, H.E. Black Carbon Pollution in Snow and Its Impact on Albedo near the Chilean Stations on the Antarctic Peninsula: First Results. *Sci. Total Environ.* **2020**, *743*, 140801. [[CrossRef](#)] [[PubMed](#)]
68. Cui, J.; Shi, T.; Zhou, Y.; Wu, D.; Wang, X.; Pu, W. Satellite-Based Radiative Forcing by Light-Absorbing Particles in Snow across the Northern Hemisphere. *Atmos. Chem. Phys.* **2021**, *21*, 269–288. [[CrossRef](#)]
69. Warren, S.G. Optical Properties of Snow. *Rev. Geophys.* **1982**, *20*, 67–89. [[CrossRef](#)]
70. Panicker, A.S.; Sandeep, K.; Gautam, A.S.; Trimbake, H.K.; Nainwal, H.C.; Beig, G.; Bisht, D.S.; Das, S. Black Carbon over a Central Himalayan Glacier (Satopanth): Pathways and Direct Radiative Impacts. *Sci. Total Environ.* **2021**, *766*, 144242. [[CrossRef](#)]

Disclaimer/Publisher's Note: The statements, opinions and data contained in all publications are solely those of the individual author(s) and contributor(s) and not of MDPI and/or the editor(s). MDPI and/or the editor(s) disclaim responsibility for any injury to people or property resulting from any ideas, methods, instructions or products referred to in the content.